Band-gap opening in graphene: A reverse-engineering approach

Joon-Suh Park[1,2,*] and Hyoung Joon Choi[1,†]
[1]*Department of Physics and IPAP, Yonsei University, Seoul 120-749, Republic of Korea*
[2]*Korea Institute of Science and Technology, Seoul 136-791, Republic of Korea*
(Received 30 April 2015; revised manuscript received 2 June 2015; published 2 July 2015)

Graphene has extremely high mobility with unique linear band dispersions at the Fermi level, referred to as the Dirac cones, but the absence of the energy gap limits its application for switching devices. To open an energy gap, theoretical studies so far have introduced certain perturbations to graphene in the real or momentum space and checked whether they open a gap at the Dirac point. Here, as a reverse approach, we directly enforce energy splittings at the Dirac point with perturbations in the minimal Hilbert space at the Dirac point and then characterize the perturbations in the real space to obtain perturbed band structures throughout the Brillouin zone. Our approach provides refined descriptions of the sublattice symmetry breaking and the intervalley scattering, distinguishing clearly the sublattice symmetry breaking without intervalley scattering, the sublattice mixing without intervalley scattering, the intervalley scattering within each sublattice, and the intersublattice intervalley scattering. For fully gapped cases, the effective mass is obtained as a function of the energy gap. Our present method can be applied to band-gap engineering of graphene-like hexagonal layered materials, in general.

DOI: 10.1103/PhysRevB.92.045402 PACS number(s): 73.22.Pr, 73.61.Wp, 71.20.−b

I. INTRODUCTION

Graphene is a two-dimensional monolayer of carbon atoms forming a honeycomb lattice [1–4], and it has drawn enormous attention from scientists and engineers due to its peculiar properties [5–9]. The basic characteristics of graphene were explored by Wallace during his research on the tight-binding description of graphite in 1947 [10]. Graphene possesses semimetallic properties with a massless dispersion and a vanishing density of states at the Fermi point [11]. The absence of an energy gap in graphene limits its application for electronic switching devices, so the issue of opening and tuning the band gap in graphene has attracted great interest. Many methods have been studied for band-gap engineering such as dopings [12,13], substrate effects [14–18], patternings [19–22], hydrogenations [23], adatoms [24], etc. Widely studied origins of the band-gap opening are the sublattice symmetry breaking [25] and the interaction between the two Dirac cones, namely, the intervalley scattering [26–28].

The sublattice symmetry breaking was studied by Semenoff [6], who considered the graphite system a diatomic system and separated the conduction and valence bands by applying an energy difference on each sublattice. This suggests the sublattice symmetry is the origin of Dirac point in graphene [11,25]. Breaking the sublattice symmetry has been studied by introducing a substrate such as boron nitride (BN) [29,30]. While graphene on top of a lattice-matched hexagonal BN has an energy gap of about 50 meV (Refs. [29,30]) resulting from different potentials on the two sublattices of graphene, the moiré structures considering the lattice mismatch of graphene and BN have energy gaps of a few meV (Ref. [30]).

Effects of the intervalley scattering have been investigated with graphene-like two-dimensional structures. Chamon [31], Hou *et al.* [32], and Lee *et al.* [33] discussed that the Kekulé distortion couples the Dirac cones at K and K' and thus results in a band-gap opening. Mañes *et al.* [34,35] demonstrated that long-wavelength perturbations could hybridize the two Dirac points and discussed that some perturbations could open an energy gap, while others could merely shift the positions of the Dirac points in the momentum space.

Theoretical studies so far have introduced certain perturbations to graphene in the real or momentum space and checked whether they split the degeneracy at the Dirac point and open an energy gap throughout the Brillouin zone (BZ). In our present work, as a reverse approach, we directly split the degeneracy at the Dirac point with perturbations in the minimal Hilbert space at the Dirac point, then characterize the perturbations in the real space, and obtain perturbed band structures throughout the BZ to check any band-gap opening. If an energy gap opens throughout the BZ or a quadratic band dispersion occurs, we obtain the effective mass as a function of the energy gap or the perturbation strength. Our theoretical study is based on a simple tight-binding method [36] for the band structures of graphene, and we choose a $\sqrt{3} \times \sqrt{3}R30^\circ$ supercell of graphene [37], which contains six carbon atoms, to consider both the sublattice symmetry breaking and the intervalley scattering. With this supercell, the Dirac cones at the K and K' points of the BZ of the unit cell are folded to the Γ point of the BZ of the supercell, forming fourfold degeneracy at the Γ point [32,34,35,38].

Our present approach can provide refined descriptions of the sublattice symmetry breaking and the intervalley scattering, distinguishing clearly (a) the sublattice symmetry breaking without intervalley scattering, (b) the sublattice mixing without intervalley scattering, (c) the intervalley scattering within each sublattice, and (d) the intersublattice intervalley scattering. We study these four perturbations and, additionally, the coexistence of perturbations (b) and (c). This paper consists of four sections. In Sec. II, we describe our tight-binding method for pristine and perturbed graphene and the step-by-step procedure of transforming perturbations in the minimal Hilbert space at the Dirac points to the real space and obtaining perturbed band structures. In Sec. III, we consider effects of five different perturbations one by one. In Sec. IV, we summarize the results.

*fieryice@kist.re.kr
†h.j.choi@yonsei.ac.kr

II. THEORETICAL FRAMEWORK

It is well known that the low-energy electronic structure near the Fermi energy in graphene is mainly from the π bond of the carbon $2p_z$ orbitals normal to the carbon plane, while carbon $2s$, $2p_x$, and $2p_y$ orbitals form planar sp^2 hybridized orbitals making the strong σ bonds of the carbon honeycomb lattice. In our present work, we are interested in the low-energy electronic structure in graphene, so we can approximately describe the electronic structure of graphene with a single-band tight-binding method considering only one $2p_z$ orbital per carbon atom and the nearest-neighbor interaction [39,40].

To describe the electronic band structure, we introduce Bloch-like extended states $\varphi_{A,\vec{k}}$ and $\varphi_{B,\vec{k}}$ of the wave vector $\vec{k}$, which are linear combinations of carbon $2p_z$ orbitals at sublattices A and B, respectively. They are defined as

$$\varphi_{A,\vec{k}} = \frac{1}{\sqrt{N}} \sum_{\vec{R}} e^{i\vec{k}\cdot(\vec{\tau}_A+\vec{R})} \varphi_{\vec{\tau}_A+\vec{R}}, \tag{1a}$$

$$\varphi_{B,\vec{k}} = \frac{1}{\sqrt{N}} \sum_{\vec{R}} e^{i\vec{k}\cdot(\vec{\tau}_B+\vec{R})} \varphi_{\vec{\tau}_B+\vec{R}}, \tag{1b}$$

where $\vec{R}$ is the position of a unit cell and $\vec{\tau}_A$ and $\vec{\tau}_B$ are positions of carbon atoms at the sublattices A and B inside a unit cell, respectively. Here, $\varphi_{\vec{\tau}+\vec{R}}$ is the carbon $2p_z$ orbital at the position $\vec{\tau}+\vec{R}$, and N is the number of unit cells in the layer. Using these extended states, an energy eigenstate $\psi_{n,\vec{k}}$ of wave vector $\vec{k}$ can be expressed as

$$\psi_{n,\vec{k}} = c_{n,\vec{k},A}\varphi_{A,\vec{k}} + c_{n,\vec{k},B}\varphi_{B,\vec{k}}, \tag{2}$$

where $c_{n,\vec{k},A}$ and $c_{n,\vec{k},B}$ are complex numbers which depend on the band index n and the wave vector $\vec{k}$. We assume that two carbon $2p_z$ orbitals are orthogonal to each other when they are associated with different carbon sites. For a minimal Hamiltonian $\hat{H}$ of unperturbed graphene, we consider only the on-site energy $\varepsilon = \langle\varphi_{\vec{\tau}+\vec{R}}|\hat{H}|\varphi_{\vec{\tau}+\vec{R}}\rangle$ and the nearest-neighbor interaction $t = \langle\varphi_{\vec{\tau}+\vec{R}}|\hat{H}|\varphi_{\vec{\tau}+\vec{R}+\vec{d}}\rangle$, with $\vec{d}$ being one of the three nearest-neighbor positions from a carbon atom. Because of the C_3 rotational symmetry around a carbon atom, t is independent of the direction of $\vec{d}$. Now we consider the Hamiltonian matrix represented with respect to $\varphi_{A,\vec{k}}$ and $\varphi_{B,\vec{k}}$. We need to consider

$$\langle\varphi_{A,\vec{k}}|\hat{H}_0|\varphi_{A,\vec{k}}\rangle = \frac{1}{N}\sum_{\vec{R},\vec{R}'} e^{i\vec{k}\cdot(\vec{R}-\vec{R}')}\langle\varphi_{\vec{\tau}_A+\vec{R}'}|\hat{H}_0|\varphi_{\vec{\tau}_A+\vec{R}}\rangle = \varepsilon, \tag{3a}$$

$$\langle\varphi_{B,\vec{k}}|\hat{H}_0|\varphi_{B,\vec{k}}\rangle = \frac{1}{N}\sum_{\vec{R},\vec{R}'} e^{i\vec{k}\cdot(\vec{R}-\vec{R}')}\langle\varphi_{\vec{\tau}_B+\vec{R}'}|\hat{H}_0|\varphi_{\vec{\tau}_B+\vec{R}}\rangle = \varepsilon, \tag{3b}$$

$$\begin{aligned}\langle\varphi_{A,\vec{k}}|\hat{H}_0|\varphi_{B,\vec{k}}\rangle &= \frac{1}{N}\sum_{\vec{R},\vec{R}'} e^{i\vec{k}\cdot(\vec{\tau}_B+\vec{R}-\vec{\tau}_A-\vec{R}')}\langle\varphi_{\vec{\tau}_A+\vec{R}'}|\hat{H}_0|\varphi_{\vec{\tau}_B+\vec{R}}\rangle \\ &= \sum_{i=1}^{3} e^{i\vec{k}\cdot\vec{d}_i}\langle\varphi_{\vec{\tau}_A}|\hat{H}_0|\varphi_{\vec{\tau}_A+\vec{d}_i}\rangle \\ &= (e^{i\vec{k}\cdot\vec{d}_1}+e^{i\vec{k}\cdot\vec{d}_2}+e^{i\vec{k}\cdot\vec{d}_3})t = \alpha(\vec{k}),\end{aligned} \tag{3c}$$

$$\langle\varphi_{B,\vec{k}}|\hat{H}_0|\varphi_{A,\vec{k}}\rangle = \alpha^*(\vec{k}), \tag{3d}$$

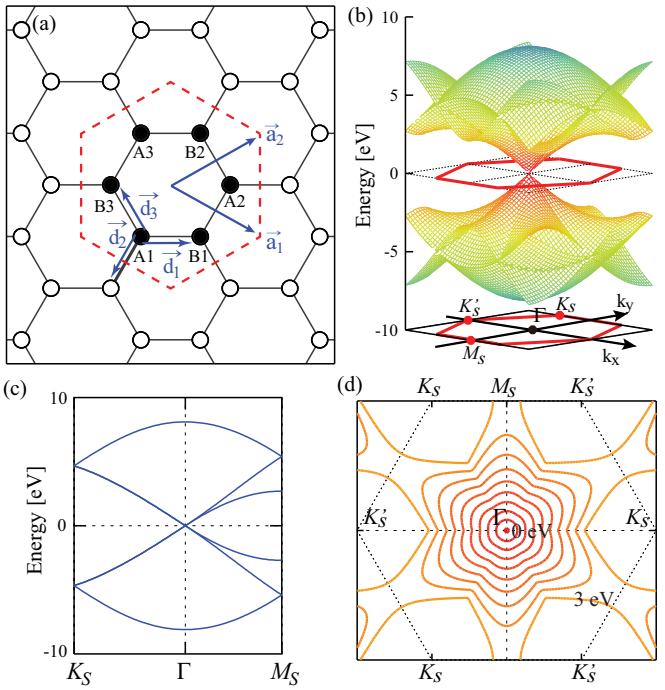

FIG. 1. (Color online) Atomic and electronic structures of pristine graphene. (a) A $\sqrt{3}\times\sqrt{3}R30^\circ$ supercell containing six carbon atoms. The dotted hexagon shows the supercell boundary. (b) Tight-binding band structure of the supercell plotted for the full BZ of the supercell. High-symmetry points are also shown. (c) Tight-binding band structure along high-symmetry lines of the supercell BZ. (b) and (c) indicate that Dirac cones are at Γ. (d) Contour plot of the lowest conduction band in the supercell BZ from 0 to 3 eV with a contour interval of 0.3 eV.

where the nearest-neighbor hopping parameter t is approximately -2.7 eV (Ref. [4]) and $\vec{d}_i$ $(i = 1,2,3)$ are relative positions of the three nearest-neighboring B sites from an A site, as shown in Fig. 1(a). With these, we can write the Hamiltonian matrix of pristine graphene for a specific wave vector $\vec{k}$ as [40]

$$\begin{aligned}H^{(0)}_{uc}(\vec{k}) &= \begin{pmatrix}\langle\varphi_{A,\vec{k}}|\hat{H}_0|\varphi_{A,\vec{k}}\rangle & \langle\varphi_{A,\vec{k}}|\hat{H}_0|\varphi_{B,\vec{k}}\rangle \\ \langle\varphi_{B,\vec{k}}|\hat{H}_0|\varphi_{A,\vec{k}}\rangle & \langle\varphi_{B,\vec{k}}|\hat{H}_0|\varphi_{B,\vec{k}}\rangle\end{pmatrix} \\ &= \begin{pmatrix}\varepsilon & \alpha(\vec{k}) \\ \alpha^*(\vec{k}) & \varepsilon\end{pmatrix}.\end{aligned} \tag{4}$$

Then by choosing ε as the reference of the energy, we have the Hamiltonian equation of unperturbed graphene:

$$\begin{pmatrix}0 & \alpha(\vec{k}) \\ \alpha^*(\vec{k}) & 0\end{pmatrix}\begin{pmatrix}c_{n,\vec{k},A} \\ c_{n,\vec{k},B}\end{pmatrix} = E_n(\vec{k})\begin{pmatrix}c_{n,\vec{k},A} \\ c_{n,\vec{k},B}\end{pmatrix}, \tag{5}$$

where $E_n(\vec{k})$ is the band energy of the wave vector $\vec{k}$ of the nth band and the corresponding energy eigenstate is given by Eq. (2). It is well known that Eq. (5) has $E_n(\vec{k}) = 0$ if $\vec{k}$ is K or K', which is equal to $-K$, of the unit-cell BZ. The $\vec{k}$ points for $E_n(\vec{k}) = 0$ are referred to as the Dirac point.

If we take the $\sqrt{3}\times\sqrt{3}R30^\circ$ supercell of graphene [Fig. 1(a)], the K and K' points of the unit-cell BZ are folded to the Γ point of the supercell BZ. Since the supercell has six carbon atoms, we define six Bloch-like extended states

$$\tilde{\varphi}_{j,\vec{k}} = \frac{1}{\sqrt{N_s}} \sum_{\vec{R}_s} e^{i\vec{k}\cdot(\vec{\tau}_j+\vec{R}_s)} \varphi_{\vec{\tau}_j+\vec{R}_s}, \tag{6}$$

where $j = A1, A2, A3, B1, B2$, and $B3$ indicate three A-site carbon atoms and three B-site carbon atoms in the supercell, respectively, as shown in Fig. 1(a). In Eq. (6), the wave vector $\vec{k}$ is in the first BZ of the supercell, N_s is the number of supercells in the crystal, which is equal to $N/3$, $\vec{R}_s$ is the position of a supercell, and $\vec{\tau}_j$ is the position of the carbon atom at the site j inside a supercell, as marked in Fig. 1(a). Using the unit-cell lattice vectors $\vec{a}_1$ and $\vec{a}_2$, the carbon atomic positions are given by $\vec{\tau}_{A1} = \frac{1}{3}(\vec{a}_1 - 2\vec{a}_2)$, $\vec{\tau}_{A2} = \frac{1}{3}(\vec{a}_1 + \vec{a}_2)$, $\vec{\tau}_{A3} = \frac{1}{3}(-2\vec{a}_1 + \vec{a}_2)$, $\vec{\tau}_{B1} = \frac{1}{3}(2\vec{a}_1 - \vec{a}_2)$, $\vec{\tau}_{B2} = \frac{1}{3}(-\vec{a}_1 + 2\vec{a}_2)$, and $\vec{\tau}_{B3} = \frac{1}{3}(-\vec{a}_1 - \vec{a}_2)$. Using $\tilde{\varphi}_{j,\vec{k}}$, a wave function $\tilde{\psi}_{n,\vec{k}}$ in the layer can be expressed as

$$\tilde{\psi}_{n,\vec{k}} = \sum_j \tilde{c}_{n,\vec{k},j} \tilde{\varphi}_{j,\vec{k}}, \tag{7}$$

where $\tilde{c}_{n,\vec{k},j}$ are complex numbers. For our $\sqrt{3}\times\sqrt{3}R30^\circ$ supercell of graphene, the tight-binding Hamiltonian is expressed as a 6×6 matrix:

$$H_{sc}^{(0)}(\vec{k}) = \begin{pmatrix} 0 & 0 & 0 & \alpha_1(\vec{k}) & \alpha_2(\vec{k}) & \alpha_3(\vec{k}) \\ 0 & 0 & 0 & \alpha_2(\vec{k}) & \alpha_3(\vec{k}) & \alpha_1(\vec{k}) \\ 0 & 0 & 0 & \alpha_3(\vec{k}) & \alpha_1(\vec{k}) & \alpha_2(\vec{k}) \\ \alpha_1^*(\vec{k}) & \alpha_2^*(\vec{k}) & \alpha_3^*(\vec{k}) & 0 & 0 & 0 \\ \alpha_2^*(\vec{k}) & \alpha_3^*(\vec{k}) & \alpha_1^*(\vec{k}) & 0 & 0 & 0 \\ \alpha_3^*(\vec{k}) & \alpha_1^*(\vec{k}) & \alpha_2^*(\vec{k}) & 0 & 0 & 0 \end{pmatrix}, \tag{8}$$

where the basis states are in the order of $\tilde{\varphi}_{A1,\vec{k}}$, $\tilde{\varphi}_{A2,\vec{k}}$, $\tilde{\varphi}_{A3,\vec{k}}$, $\tilde{\varphi}_{B1,\vec{k}}$, $\tilde{\varphi}_{B2,\vec{k}}$, and $\tilde{\varphi}_{B3,\vec{k}}$ and $\alpha_l(\vec{k}) \equiv t \cdot e^{i\vec{k}\cdot\vec{d}_l}$ for $l = 1,2,3$. With this Hamiltonian, we have the eigenvalue equation for unperturbed graphene:

$$H_{sc}^{(0)}(\vec{k}) \begin{pmatrix} \tilde{c}_{n,\vec{k},A1} \\ \tilde{c}_{n,\vec{k},A2} \\ \tilde{c}_{n,\vec{k},A3} \\ \tilde{c}_{n,\vec{k},B1} \\ \tilde{c}_{n,\vec{k},B2} \\ \tilde{c}_{n,\vec{k},B3} \end{pmatrix} = E_n^{sc}(\vec{k}) \begin{pmatrix} \tilde{c}_{n,\vec{k},A1} \\ \tilde{c}_{n,\vec{k},A2} \\ \tilde{c}_{n,\vec{k},A3} \\ \tilde{c}_{n,\vec{k},B1} \\ \tilde{c}_{n,\vec{k},B2} \\ \tilde{c}_{n,\vec{k},B3} \end{pmatrix}, \tag{9}$$

where $E_n^{sc}(\vec{k})$ is the nth band energy for the wave vector $\vec{k}$ in the supercell BZ and the corresponding wave function is given by Eq. (7).

Figures 1(b) and 1(c) show the $\sqrt{3}\times\sqrt{3}R30^\circ$ supercell band structure of unperturbed graphene obtained from Eq. (9). Because of the band-folding effect, $E_n^{sc}(\vec{k}) = 0$ occurs at $\vec{k} = 0$ of the supercell BZ, which has one-third the area of the BZ of the unit cell rotated by 30°. At the Γ point of the supercell BZ, where $\vec{k} = 0$, four states are degenerate at zero energy, one state is located at $E = 3t$, and one state is at $E = -3t$. The four degenerate states are the states at the Dirac points at the K and K' points of the unit-cell BZ, and the other two states are those at the Γ point of the unit-cell BZ.

When we have a perturbation which has the periodicity of the supercell, the perturbed Hamiltonian will be generally given by

$$H_{sc}(\vec{k}) = \begin{pmatrix} D_{A1} & \beta_{A1,A2}(\vec{k}) & \beta_{A1,A3}(\vec{k}) & \alpha_{A1,B1}(\vec{k}) & \alpha_{A1,B2}(\vec{k}) & \alpha_{A1,B3}(\vec{k}) \\ \beta_{A1,A2}^*(\vec{k}) & D_{A2} & \beta_{A2,A3}(\vec{k}) & \alpha_{A2,B1}(\vec{k}) & \alpha_{A2,B2}(\vec{k}) & \alpha_{A2,B3}(\vec{k}) \\ \beta_{A1,A3}^*(\vec{k}) & \beta_{A2,A3}^*(\vec{k}) & D_{A3} & \alpha_{A3,B1}(\vec{k}) & \alpha_{A3,B2}(\vec{k}) & \alpha_{A3,B3}(\vec{k}) \\ \alpha_{A1,B1}^*(\vec{k}) & \alpha_{A2,B1}^*(\vec{k}) & \alpha_{A3,B1}^*(\vec{k}) & D_{B1} & \beta_{B1,B2}(\vec{k}) & \beta_{B1,B3}(\vec{k}) \\ \alpha_{A1,B2}^*(\vec{k}) & \alpha_{A2,B2}^*(\vec{k}) & \alpha_{A3,B2}^*(\vec{k}) & \beta_{B1,B2}^*(\vec{k}) & D_{B2} & \beta_{B2,B3}(\vec{k}) \\ \alpha_{A1,B3}^*(\vec{k}) & \alpha_{A2,B3}^*(\vec{k}) & \alpha_{A3,B3}^*(\vec{k}) & \beta_{B1,B3}^*(\vec{k}) & \beta_{B2,B3}^*(\vec{k}) & D_{B3} \end{pmatrix}, \tag{10}$$

where D_j are diagonal elements, $\alpha_{i,j}(\vec{k})$ are off-diagonal elements between the two sublattices, and $\beta_{i,j}(\vec{k})$ are off-diagonal elements within each sublattice. The diagonal elements are independent of $\vec{k}$ unless we consider hopping between the fourth-nearest neighbors. If we consider only on-site energies and hopping energies between the nearest neighbors and between the

next-nearest neighbors, the Hamiltonian is given by

$$H_{sc}(\vec{k}) = \begin{pmatrix} D_{A1} & t_{A1,A2}f(-\vec{k}) & t_{A1,A3}f(\vec{k}) & t_{A1,B1}e^{i\vec{k}\cdot\vec{d}_1} & t_{A1,B2}e^{i\vec{k}\cdot\vec{d}_2} & t_{A1,B3}e^{i\vec{k}\cdot\vec{d}_3} \\ t_{A1,A2}f(\vec{k}) & D_{A2} & t_{A2,A3}f(-\vec{k}) & t_{A2,B1}e^{i\vec{k}\cdot\vec{d}_2} & t_{A2,B2}e^{i\vec{k}\cdot\vec{d}_3} & t_{A2,B3}e^{i\vec{k}\cdot\vec{d}_1} \\ t_{A1,A3}f(-\vec{k}) & t_{A2,A3}f(\vec{k}) & D_{A3} & t_{A3,B1}e^{i\vec{k}\cdot\vec{d}_3} & t_{A3,B2}e^{i\vec{k}\cdot\vec{d}_1} & t_{A3,B3}e^{i\vec{k}\cdot\vec{d}_2} \\ t_{A1,B1}e^{-i\vec{k}\cdot\vec{d}_1} & t_{A2,B1}e^{-i\vec{k}\cdot\vec{d}_2} & t_{A3,B1}e^{-i\vec{k}\cdot\vec{d}_3} & D_{B1} & t_{B1,B2}f(\vec{k}) & t_{B1,B3}f(-\vec{k}) \\ t_{A1,B2}e^{-i\vec{k}\cdot\vec{d}_2} & t_{A2,B2}e^{-i\vec{k}\cdot\vec{d}_3} & t_{A3,B2}e^{-i\vec{k}\cdot\vec{d}_1} & t_{B1,B2}f(-\vec{k}) & D_{B2} & t_{B2,B3}f(\vec{k}) \\ t_{A1,B3}e^{-i\vec{k}\cdot\vec{d}_3} & t_{A2,B3}e^{-i\vec{k}\cdot\vec{d}_1} & t_{A3,B3}e^{-i\vec{k}\cdot\vec{d}_2} & t_{B1,B3}f(\vec{k}) & t_{B2,B3}f(-\vec{k}) & D_{B3} \end{pmatrix}, \tag{11}$$

where $f(\vec{k}) = e^{i\vec{k}\cdot\vec{a}_1} + e^{-i\vec{k}\cdot\vec{a}_2} + e^{i\vec{k}\cdot(-\vec{a}_1+\vec{a}_2)}$ and $f(-\vec{k}) = f^*(\vec{k})$. Here, $t_{i,j}$ is the hopping energy from site i to site j, and we assumed that hopping energies between the next-nearest neighbors have the C_3 symmetry; that is, the next-nearest-neighbor hopping energy is invariant under 120° rotation. Thus, within this model, the Hamiltonian is determined by six on-site energies, nine hopping energies between the nearest neighbors, and six hopping energies between the next-nearest neighbors. When we consider the Hamiltonian for $\vec{k} = 0$, which is

$$H_{sc}(\vec{k}=0) = \begin{pmatrix} D_{A1} & 3t_{A1,A2} & 3t_{A1,A3} & t_{A1,B1} & t_{A1,B2} & t_{A1,B3} \\ 3t_{A1,A2} & D_{A2} & 3t_{A2,A3} & t_{A2,B1} & t_{A2,B2} & t_{A2,B3} \\ 3t_{A1,A3} & 3t_{A2,A3} & D_{A3} & t_{A3,B1} & t_{A3,B2} & t_{A3,B3} \\ t_{A1,B1} & t_{A2,B1} & t_{A3,B1} & D_{B1} & 3t_{B1,B2} & 3t_{B1,B3} \\ t_{A1,B2} & t_{A2,B2} & t_{A3,B2} & 3t_{B1,B2} & D_{B2} & 3t_{B2,B3} \\ t_{A1,B3} & t_{A2,B3} & t_{A3,B3} & 3t_{B1,B3} & 3t_{B2,B3} & D_{B3} \end{pmatrix}, \tag{12}$$

each matrix element depends on only one of the on-site or the hopping energies. Thus, if the Hamiltonian for $\vec{k} = 0$ is given, the Hamiltonian can be generated for any $\vec{k}$ within the model, from which the perturbed band structure can be obtained for the full BZ.

To analyze effects of perturbations on the electronic structure in the $\sqrt{3} \times \sqrt{3}R30^\circ$ supercell of graphene, we introduce linear combinations of $\tilde{\varphi}_{j,\vec{k}=0}$ as [32,34,35,38,41]

$$\xi_{A,K} = \frac{1}{\sqrt{3}}(e^{i\vec{K}\cdot\vec{\tau}_{A1}}\tilde{\varphi}_{A1,\vec{k}=0} + e^{i\vec{K}\cdot\vec{\tau}_{A2}}\tilde{\varphi}_{A2,\vec{k}=0} + e^{i\vec{K}\cdot\vec{\tau}_{A3}}\tilde{\varphi}_{A3,\vec{k}=0}), \quad \xi_{A,K'} = \frac{1}{\sqrt{3}}(e^{i\vec{K}'\cdot\vec{\tau}_{A1}}\tilde{\varphi}_{A1,\vec{k}=0} + e^{i\vec{K}'\cdot\vec{\tau}_{A2}}\tilde{\varphi}_{A2,\vec{k}=0} + e^{i\vec{K}'\cdot\vec{\tau}_{A3}}\tilde{\varphi}_{A3,\vec{k}=0}),$$

$$\xi_{B,K} = \frac{1}{\sqrt{3}}(e^{i\vec{K}\cdot\vec{\tau}_{B1}}\tilde{\varphi}_{B1,\vec{k}=0} + e^{i\vec{K}\cdot\vec{\tau}_{B2}}\tilde{\varphi}_{B2,\vec{k}=0} + e^{i\vec{K}\cdot\vec{\tau}_{B3}}\tilde{\varphi}_{B3,\vec{k}=0}), \quad \xi_{B,K'} = \frac{1}{\sqrt{3}}(e^{i\vec{K}'\cdot\vec{\tau}_{B1}}\tilde{\varphi}_{B1,\vec{k}=0} + e^{i\vec{K}'\cdot\vec{\tau}_{B2}}\tilde{\varphi}_{B2,\vec{k}=0} + e^{i\vec{K}'\cdot\vec{\tau}_{B3}}\tilde{\varphi}_{B3,\vec{k}=0}),$$

$$\xi_{A,\Gamma} = \frac{1}{\sqrt{3}}(\tilde{\varphi}_{A1,\vec{k}=0} + \tilde{\varphi}_{A2,\vec{k}=0} + \tilde{\varphi}_{A3,\vec{k}=0}), \quad \xi_{B,\Gamma} = \frac{1}{\sqrt{3}}(\tilde{\varphi}_{B1,\vec{k}=0} + \tilde{\varphi}_{B2,\vec{k}=0} + \tilde{\varphi}_{B3,\vec{k}=0}). \tag{13}$$

Using $\vec{\tau}_{A1} = \frac{1}{3}(\vec{a}_1 - 2\vec{a}_2), \vec{\tau}_{A2} = \frac{1}{3}(\vec{a}_1 + \vec{a}_2), \vec{\tau}_{A3} = \frac{1}{3}(-2\vec{a}_1 + \vec{a}_2), \vec{\tau}_{B1} = \frac{1}{3}(2\vec{a}_1 - \vec{a}_2), \vec{\tau}_{B2} = \frac{1}{3}(-\vec{a}_1 + 2\vec{a}_2), \vec{\tau}_{B3} = \frac{1}{3}(-\vec{a}_1 - \vec{a}_2)$, $\vec{K} = \frac{1}{3}(2\vec{b}_1 + \vec{b}_2)$, and $\vec{K}' = \frac{1}{3}(\vec{b}_1 + 2\vec{b}_2)$, where $\vec{b}_1$ and $\vec{b}_2$ are the reciprocal lattice vectors of the unit cell, we have

$$\xi_{A,K} = \frac{1}{\sqrt{3}}(\tilde{\varphi}_{A1,\vec{k}=0} + e^{i\frac{2\pi}{3}}\tilde{\varphi}_{A2,\vec{k}=0} + e^{-i\frac{2\pi}{3}}\tilde{\varphi}_{A3,\vec{k}=0}), \quad \xi_{A,K'} = \frac{1}{\sqrt{3}}(e^{-i\frac{2\pi}{3}}\tilde{\varphi}_{A1,\vec{k}=0} + e^{i\frac{2\pi}{3}}\tilde{\varphi}_{A2,\vec{k}=0} + \tilde{\varphi}_{A3,\vec{k}=0}),$$

$$\xi_{B,K} = \frac{1}{\sqrt{3}}(e^{i\frac{2\pi}{3}}\tilde{\varphi}_{B1,\vec{k}=0} + \tilde{\varphi}_{B2,\vec{k}=0} + e^{-i\frac{2\pi}{3}}\tilde{\varphi}_{B3,\vec{k}=0}), \quad \xi_{B,K'} = \frac{1}{\sqrt{3}}(\tilde{\varphi}_{B1,\vec{k}=0} + e^{i\frac{2\pi}{3}}\tilde{\varphi}_{B2,\vec{k}=0} + e^{-i\frac{2\pi}{3}}\tilde{\varphi}_{B3,\vec{k}=0}),$$

$$\xi_{A,\Gamma} = \frac{1}{\sqrt{3}}(\tilde{\varphi}_{A1,\vec{k}=0} + \tilde{\varphi}_{A2,\vec{k}=0} + \tilde{\varphi}_{A3,\vec{k}=0}), \quad \xi_{B,\Gamma} = \frac{1}{\sqrt{3}}(\tilde{\varphi}_{B1,\vec{k}=0} + \tilde{\varphi}_{B2,\vec{k}=0} + \tilde{\varphi}_{B3,\vec{k}=0}). \tag{14}$$

From these relations, we define a unitary matrix U_{ij} such that $\xi_j = \sum_i U_{ij}\tilde{\varphi}_{i,\vec{k}=0}$. Using this unitary matrix,

$$U = \frac{1}{\sqrt{3}}\begin{pmatrix} 1 & e^{-i\frac{2\pi}{3}} & 0 & 0 & 1 & 0 \\ e^{i\frac{2\pi}{3}} & e^{i\frac{2\pi}{3}} & 0 & 0 & 1 & 0 \\ e^{-i\frac{2\pi}{3}} & 1 & 0 & 0 & 1 & 0 \\ 0 & 0 & e^{i\frac{2\pi}{3}} & 1 & 0 & 1 \\ 0 & 0 & 1 & e^{i\frac{2\pi}{3}} & 0 & 1 \\ 0 & 0 & e^{-i\frac{2\pi}{3}} & e^{i\frac{2\pi}{3}} & 0 & 1 \end{pmatrix}, \tag{15}$$

the Hamiltonian matrix in the ξ basis, $\mathcal{H}_{sc}^{(\xi)}$, is

$$\left(\mathcal{H}_{sc}^{(\xi)}\right)_{ij} = \langle\xi_i|\hat{H}|\xi_j\rangle = \sum_{m,n} U_{mi}^*\langle\tilde{\varphi}_{m,\vec{k}=0}|\hat{H}|\tilde{\varphi}_{n,\vec{k}=0}\rangle U_{nj}$$
$$= \sum_{m,n} U_{mi}^*(H_{sc}(\vec{k}=0))_{mn}U_{nj}. \tag{16}$$

Here, we define $\mathcal{H}_{sc}^{(\xi)}$ only for $\vec{k} = 0$. The inverse transformation is

$$[H_{sc}(\vec{k}=0)]_{ij} = \sum_{m,n} U_{im}\left(\mathcal{H}_{sc}^{(\xi)}\right)_{mn}U_{jn}^*. \tag{17}$$

Without perturbation, the Hamiltonian matrix in the ξ basis is

$$\mathcal{H}_{sc}^{(\xi)} = \begin{pmatrix} 0 & 0 & 0 & 0 & 0 & 0 \\ 0 & 0 & 0 & 0 & 0 & 0 \\ 0 & 0 & 0 & 0 & 0 & 0 \\ 0 & 0 & 0 & 0 & 0 & 0 \\ 0 & 0 & 0 & 0 & 0 & 3t \\ 0 & 0 & 0 & 0 & 3t & 0 \end{pmatrix}, \quad (18)$$

where the basis states are in the order of $\xi_{A,K}$, $\xi_{A,K'}$, $\xi_{B,K}$, $\xi_{B,K'}$, $\xi_{A,\Gamma}$, and $\xi_{B,\Gamma}$. Here, the top left 4×4 block of $\mathcal{H}_{sc}^{(\xi)}$ for $\xi_{A,K}$, $\xi_{A,K'}$, $\xi_{B,K}$, and $\xi_{B,K'}$ is a null matrix because the four states span the fourfold degeneracy whose energy is set to zero. It is necessary to introduce nonzero matrix elements in this 4×4 block in order to perturb the fourfold degeneracy at the Fermi energy.

In the next section, for perturbed graphene, we will introduce nonzero matrix elements in the top left 4×4 block of $\mathcal{H}_{sc}^{(\xi)}$ of Eq. (18) for $\xi_{A,K}$, $\xi_{A,K'}$, $\xi_{B,K}$, and $\xi_{B,K'}$. Then we will transform the 6×6 Hamiltonian $\mathcal{H}_{sc}^{(\xi)}$ of Eq. (18) to $H_{sc}(\vec{k}=0)$ of Eq. (12) with respect to the basis of $\tilde{\varphi}_{A1,\vec{k}=0}$, $\tilde{\varphi}_{A2,\vec{k}=0}$, $\tilde{\varphi}_{A3,\vec{k}=0}$, $\tilde{\varphi}_{B1,\vec{k}=0}$, $\tilde{\varphi}_{B2,\vec{k}=0}$, and $\tilde{\varphi}_{B3,\vec{k}=0}$. From $H_{sc}(\vec{k}=0)$, we generate $H_{sc}(\vec{k})$ for any $\vec{k}$ in the whole BZ using Eq. (11), diagonalize it to obtain the band structure throughout the BZ, and find the effects on the Dirac cones. In our method, we clearly categorize perturbations by introducing them in the basis of $\xi_{A,K}$, $\xi_{A,K'}$, $\xi_{B,K}$, and $\xi_{B,K'}$, determine tight-binding parameters for the perturbations, and find their effects on the electronic structure in the whole BZ.

In our present work, we consider five different perturbations: (a) the sublattice symmetry breaking without intervalley scattering, (b) the sublattice mixing without intervalley scattering, (c) the intervalley scattering within each sublattice, (d) the coexistence of the sublattice mixing without intervalley scattering and the intervalley scattering within each sublattice, and (e) the intersublattice intervalley scattering. In the next section, we will describe these perturbations and present their effects on the electronic structure.

III. RESULTS

A. Sublattice symmetry breaking without intervalley scattering

In this section, we consider a perturbation which produces a sublattice symmetry breaking without intervalley scattering. Since the Dirac cones of graphene originate from the sublattice symmetry [25], breaking the sublattice symmetry can open an energy gap at the Dirac point. Such symmetry breaking has been studied, for example, with graphene on top of a lattice-matched hexagonal boron nitride [29,30] and with large superstructures considering the lattice mismatch of graphene and boron nitride [30]. In the lattice-matched case, the lowest-energy configuration has boron atoms under carbon atoms and nitrogen atoms under the centers of carbon hexagons [29,30], breaking the sublattice symmetry of graphene.

We generate the sublattice symmetry breaking without intervalley scattering by differentiating the two sublattices with different diagonal elements in the ξ-basis Hamiltonian matrix at the Γ point. For simplicity, we introduce a diagonal perturbation Δ for only the $\xi_{A,K}$ and $\xi_{A,K'}$ states. Then, our perturbed Hamiltonian at the Γ point is

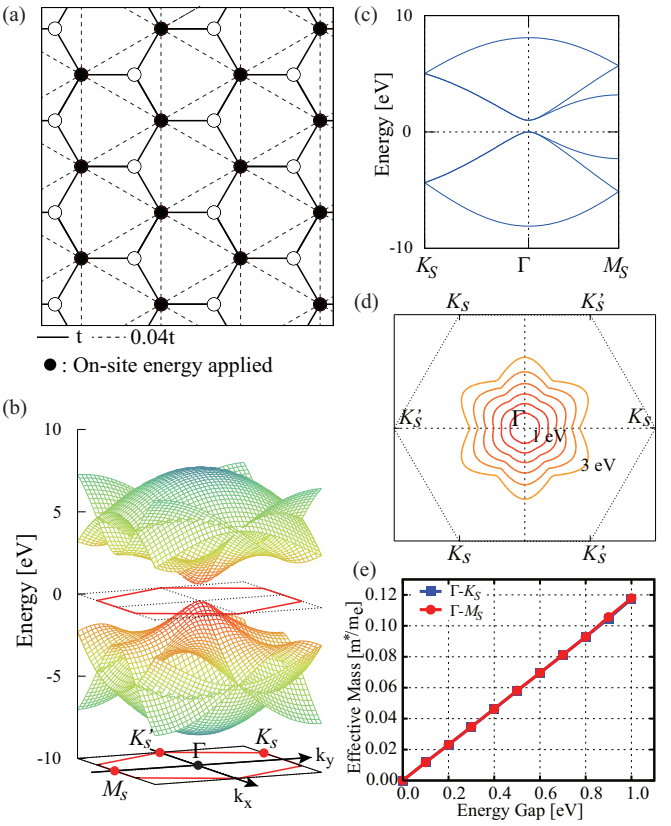

FIG. 2. (Color online) Graphene with the sublattice symmetry breaking without intervalley scattering. (a) Schematic representation of the perturbed Hamiltonian (21) with $\Delta = 1.0$ eV. Solid dots represent nonzero on-site energy ($=\frac{2}{3}\Delta$) at carbon sites, and dotted lines represent nonzero next-nearest-neighbor hopping matrix elements ($=-\frac{1}{9}\Delta = 0.04\,t$). Solid lines represent the nearest-neighbor-neighbor hopping matrix elements, $t = -2.7$ eV. (b) Tight-binding band structure of perturbed graphene in the full BZ of the supercell. (c) Tight-binding band structure of perturbed graphene along high-symmetry lines. (d) Contour plot of the lowest conduction band from 1 to 3 eV with a contour interval of 0.3 eV. (e) The effective mass of the lowest conduction band at Γ as a function of the energy gap ($=\Delta$). The effective mass in the Γ-K_S direction is the same as that in the Γ-M_S direction.

$$\mathcal{H}_{sc}^{(\xi)} = \begin{pmatrix} \Delta & 0 & 0 & 0 & 0 & 0 \\ 0 & \Delta & 0 & 0 & 0 & 0 \\ 0 & 0 & 0 & 0 & 0 & 0 \\ 0 & 0 & 0 & 0 & 0 & 0 \\ 0 & 0 & 0 & 0 & 0 & 3t \\ 0 & 0 & 0 & 0 & 3t & 0 \end{pmatrix}. \quad (19)$$

Here, the perturbation simply lifts the fourfold degeneracy into two sets of double degeneracy without making any intersublattice or intervalley interaction. By the unitary transformation, $[H_{sc}(\vec{k}=0)]_{ij} = \sum_{m,n} U_{im}(\mathcal{H}_{sc}^{(\xi)})_{mn}U_{jn}^*$, we can obtain the

$\tilde{\varphi}$-basis Hamiltonian $H_{sc}(\vec{k}=0)$:

$$H_{sc}(\vec{k}=0)=\begin{pmatrix} \frac{2}{3}\Delta & -\frac{1}{3}\Delta & -\frac{1}{3}\Delta & t & t & t \\ -\frac{1}{3}\Delta & \frac{2}{3}\Delta & -\frac{1}{3}\Delta & t & t & t \\ -\frac{1}{3}\Delta & -\frac{1}{3}\Delta & \frac{2}{3}\Delta & t & t & t \\ t & t & t & 0 & 0 & 0 \\ t & t & t & 0 & 0 & 0 \\ t & t & t & 0 & 0 & 0 \end{pmatrix}. \tag{20}$$

This Hamiltonian matrix shows that the diagonal perturbation Δ for the $\xi_{A,K}$ and $\xi_{A,K'}$ states corresponds to introducing the on-site energy value of $\frac{2}{3}\Delta$ on the A sublattice and the hopping energy of $-\frac{1}{9}\Delta$ between the next-nearest neighbors of the A sublattice. Figure 2(a) shows this perturbation schematically in the honeycomb lattice. From the Hamiltonian (20), it is straightforward to obtain the Hamiltonian for a k point in the BZ:

$$H_{sc}(\vec{k})=\begin{pmatrix} \frac{2}{3}\Delta & -\frac{\Delta}{9}f(-\vec{k}) & -\frac{\Delta}{9}f(\vec{k}) & te^{i\vec{k}\cdot\vec{d}_1} & te^{i\vec{k}\cdot\vec{d}_2} & te^{i\vec{k}\cdot\vec{d}_3} \\ -\frac{\Delta}{9}f(\vec{k}) & \frac{2}{3}\Delta & -\frac{\Delta}{9}f(-\vec{k}) & te^{i\vec{k}\cdot\vec{d}_2} & te^{i\vec{k}\cdot\vec{d}_3} & te^{i\vec{k}\cdot\vec{d}_1} \\ -\frac{\Delta}{9}f(-\vec{k}) & -\frac{\Delta}{9}f(\vec{k}) & \frac{2}{3}\Delta & te^{i\vec{k}\cdot\vec{d}_3} & te^{i\vec{k}\cdot\vec{d}_1} & te^{i\vec{k}\cdot\vec{d}_2} \\ te^{-i\vec{k}\cdot\vec{d}_1} & te^{-i\vec{k}\cdot\vec{d}_2} & te^{-i\vec{k}\cdot\vec{d}_3} & 0 & 0 & 0 \\ te^{-i\vec{k}\cdot\vec{d}_2} & te^{-i\vec{k}\cdot\vec{d}_3} & te^{-i\vec{k}\cdot\vec{d}_1} & 0 & 0 & 0 \\ te^{-i\vec{k}\cdot\vec{d}_3} & te^{-i\vec{k}\cdot\vec{d}_1} & te^{-i\vec{k}\cdot\vec{d}_2} & 0 & 0 & 0 \end{pmatrix}, \tag{21}$$

from which we obtain the perturbed band structure.

Figures 2(b) and 2(c) show the obtained electronic band structure when $\Delta = 1.0$ eV. The band gap at the Dirac point is 1.0 eV simply because Δ is the perturbation strength which we introduced to shift the band energies of the A-sublattice states at the Dirac point. With the band-gap opening, we can calculate the effective mass m^*,

$$m^* = \hbar^2\left(\frac{d^2E}{dk^2}\right)^{-1}, \tag{22}$$

as a function of the perturbation strength Δ, which is equal to the energy gap. The calculated effective mass of the lowest conduction band at Γ increases with the energy gap $E_g(=\Delta)$, as plotted in Fig. 2(e). By analytic calculations, we can derive

$$m^* = \frac{6\hbar^2 E_g}{|\vec{a}_1|^2\left(9t^2 - E_g^2\right)}, \tag{23}$$

which is in good agreement with the numerical results shown in Fig. 2(e).

B. Sublattice mixing without intervalley scattering

As a perturbation other than the sublattice symmetry breaking, we consider, in this section, a perturbation which mixes A and B sublattices without making any intervalley scattering. The perturbed ξ-based Hamiltonian is

$$\mathcal{H}_{sc}^{(\xi)}=\begin{pmatrix} 0 & 0 & \Delta_1 & 0 & 0 & 0 \\ 0 & 0 & 0 & \Delta_2 & 0 & 0 \\ \Delta_1^* & 0 & 0 & 0 & 0 & 0 \\ 0 & \Delta_2^* & 0 & 0 & 0 & 0 \\ 0 & 0 & 0 & 0 & 0 & 3t \\ 0 & 0 & 0 & 0 & 3t & 0 \end{pmatrix}. \tag{24}$$

As can be seen from the Hamiltonian matrix, this perturbation represents mixing between different sublattices within each K or K'. By the unitary transformation, $[H_{sc}(\vec{k}=0)]_{ij} = \sum_{m,n} U_{im}(\mathcal{H}_{sc}^{(\xi)})_{mn}U_{jn}^*$, we express the Hamiltonian at Γ using the $\tilde{\varphi}$ basis:

$$H_{sc}(\vec{k}=0)=\begin{pmatrix} 0 & 0 & 0 & \lambda_1+t & \lambda_2+t & \lambda_3+t \\ 0 & 0 & 0 & \lambda_2+t & \lambda_3+t & \lambda_1+t \\ 0 & 0 & 0 & \lambda_3+t & \lambda_1+t & \lambda_2+t \\ \lambda_1^*+t & \lambda_2^*+t & \lambda_3^*+t & 0 & 0 & 0 \\ \lambda_2^*+t & \lambda_3^*+t & \lambda_1^*+t & 0 & 0 & 0 \\ \lambda_3^*+t & \lambda_1^*+t & \lambda_2^*+t & 0 & 0 & 0 \end{pmatrix}, \tag{25}$$

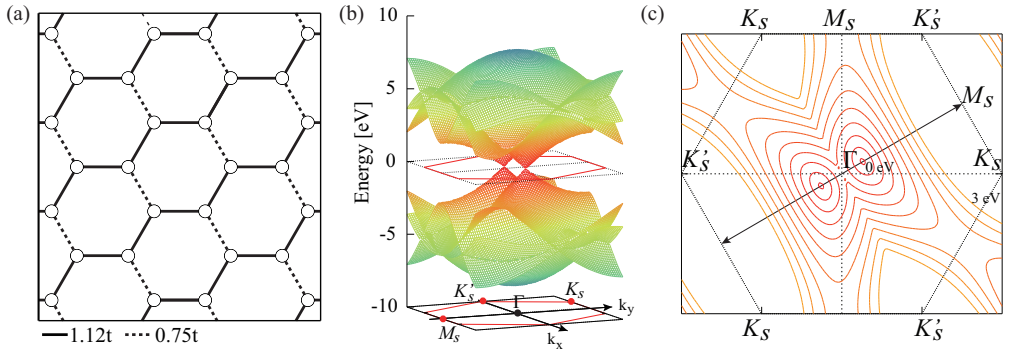

FIG. 3. (Color online) Graphene with the sublattice mixing without intervalley scattering. (a) Schematic representation of the perturbed Hamiltonian (27) with $\Delta_1 = e^{-i\frac{2\pi}{3}}\Delta_2$ and $\Delta_2 = 1$ eV. (Δ_1 is complex and Δ_2 is real.) The solid and dotted lines show variation of the nearest-neighbor hopping matrix elements, which are $1.12t$ and $0.75t$, respectively. (b) Tight-binding band structure of perturbed graphene in the full BZ of the supercell. (c) Contour plot of the lowest conduction band from 0 to 3 eV with a contour interval of 0.3 eV. The arrows indicate the directions in which the Dirac cones are shifted.

where the elements in the nearest-neighbor hopping energies are abbreviated as

$$\lambda_1 = \tfrac{1}{3}e^{-i\frac{2\pi}{3}}(\Delta_1 + \Delta_2), \tag{26a}$$

$$\lambda_2 = \tfrac{1}{3}\left(\Delta_1 + e^{i\frac{2\pi}{3}}\Delta_2\right), \tag{26b}$$

$$\lambda_3 = \tfrac{1}{3}\left(e^{i\frac{2\pi}{3}}\Delta_1 + \Delta_2\right), \tag{26c}$$

which should be real numbers to make hopping matrix elements real. Extending this Hamiltonian at Γ to a k point in the BZ gives

$$H_{sc}(\vec{k}) = \begin{pmatrix} 0 & 0 & 0 & (\lambda_1+t)e^{i\vec{k}\cdot\vec{d}_1} & (\lambda_2+t)e^{i\vec{k}\cdot\vec{d}_2} & (\lambda_3+t)e^{i\vec{k}\cdot\vec{d}_3} \\ 0 & 0 & 0 & (\lambda_2+t)e^{i\vec{k}\cdot\vec{d}_2} & (\lambda_3+t)e^{i\vec{k}\cdot\vec{d}_3} & (\lambda_1+t)e^{i\vec{k}\cdot\vec{d}_1} \\ 0 & 0 & 0 & (\lambda_3+t)e^{i\vec{k}\cdot\vec{d}_3} & (\lambda_1+t)e^{i\vec{k}\cdot\vec{d}_1} & (\lambda_2+t)e^{i\vec{k}\cdot\vec{d}_2} \\ (\lambda_1^*+t)e^{-i\vec{k}\cdot\vec{d}_1} & (\lambda_2^*+t)e^{-i\vec{k}\cdot\vec{d}_2} & (\lambda_3^*+t)e^{-i\vec{k}\cdot\vec{d}_3} & 0 & 0 & 0 \\ (\lambda_2^*+t)e^{-i\vec{k}\cdot\vec{d}_2} & (\lambda_3^*+t)e^{-i\vec{k}\cdot\vec{d}_3} & (\lambda_1^*+t)e^{-i\vec{k}\cdot\vec{d}_1} & 0 & 0 & 0 \\ (\lambda_3^*+t)e^{-i\vec{k}\cdot\vec{d}_3} & (\lambda_1^*+t)e^{-i\vec{k}\cdot\vec{d}_1} & (\lambda_2^*+t)e^{-i\vec{k}\cdot\vec{d}_2} & 0 & 0 & 0 \end{pmatrix}. \tag{27}$$

In the case that Δ_1 is equal to $|\Delta_2|$, $\Delta_2 = e^{-i\frac{2\pi}{3}}\Delta_1$ makes all hopping energies real, and in the case that Δ_2 is equal to $|\Delta_1|$, $\Delta_1 = e^{-i\frac{2\pi}{3}}\Delta_2$ makes all hopping energies real. Figure 3(a) shows the nearest-neighbor hopping energies of the perturbed system for $\Delta_1 = e^{-i\frac{2\pi}{3}}\Delta_2$ and $\Delta_2 = 1$ eV, and Fig. 3(b) shows the calculated band structure of this system. This perturbation certainly breaks the fourfold degeneracy at the Γ point, but it does not open an energy gap. The Dirac points are shifted from their original positions toward the M_S point, as shown in Fig. 3(c), and the shapes of the Dirac cones are deformed. One way to induce such changes in the hopping matrix elements is to apply a uniaxial strain. Our present results are consistent with previous reports that a uniaxial strain does not open a gap [42,43] but causes splitting at the Raman G peak [44] and shifts the Dirac cones away from the K point in the BZ [45].

C. Intervalley scattering within each sublattice

We consider a perturbation which produce intervalley scattering within each sublattice. The perturbed ξ-based Hamiltonian is

$$\mathcal{H}_{sc}^{(\xi)} = \begin{pmatrix} 0 & \Delta_3 & 0 & 0 & 0 & 0 \\ \Delta_3^* & 0 & 0 & 0 & 0 & 0 \\ 0 & 0 & 0 & \Delta_4 & 0 & 0 \\ 0 & 0 & \Delta_4^* & 0 & 0 & 0 \\ 0 & 0 & 0 & 0 & 0 & 3t \\ 0 & 0 & 0 & 0 & 3t & 0 \end{pmatrix}, \tag{28}$$

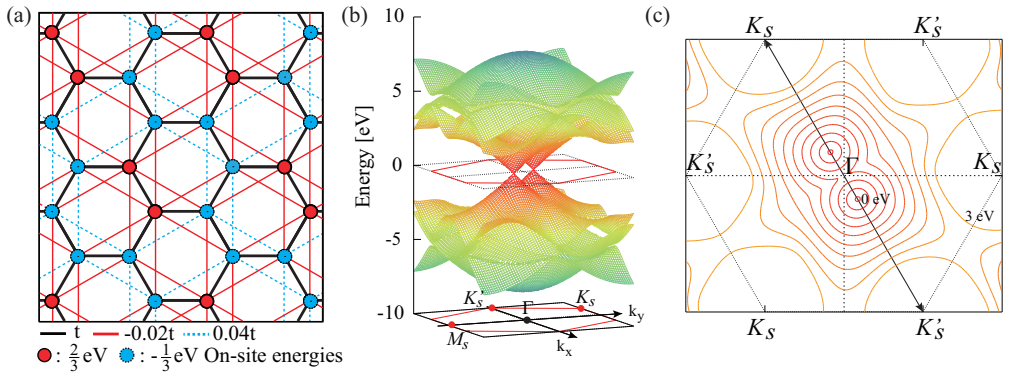

FIG. 4. (Color online) Graphene with the intervalley scattering within each sublattice. (a) Schematic representation of the perturbed Hamiltonian (31) with $\Delta_1 = e^{-i\frac{2\pi}{3}}\Delta_2$ and $\Delta_2 = 1$ eV. (Δ_1 is complex and Δ_2 is real.) The red solid and blue dotted lines show variation of the next-nearest-neighbor hopping matrix elements, which are $-0.02t$ and $0.04t$, respectively. Red and blue dots represent variation of on-site energies, which are $\frac{2}{3}$ and $-\frac{1}{3}$ eV, respectively. (b) Tight-binding band structure of perturbed graphene in the full BZ of the supercell. (c) Contour plot of the lowest conduction band from 0 to 3 eV with a contour interval of 0.3 eV. The arrows indicate the directions in which the Dirac cones are shifted.

which induces mixing between states at the K and K' points of the same sublattice. By the unitary transformation, $[H_{sc}(\vec{k} = 0)] = \sum_{m,n} U_{im}(\mathcal{H}_{sc}^{(\xi)})_{mn}U_{jn}^*$, we express the Hamiltonian using the $\tilde{\varphi}$ basis:

$$H_{sc}(\vec{k}=0) = \begin{pmatrix} \rho_2(\Delta_3) & \rho_3(\Delta_3) & \rho_1(\Delta_3) & t & t & t \\ \rho_3(\Delta_3) & \rho_1(\Delta_3) & \rho_2(\Delta_3) & t & t & t \\ \rho_1(\Delta_3) & \rho_2(\Delta_3) & \rho_3(\Delta_3) & t & t & t \\ t & t & t & \rho_2(\Delta_4) & \rho_1(\Delta_4) & \rho_3(\Delta_4) \\ t & t & t & \rho_1(\Delta_4) & \rho_3(\Delta_4) & \rho_2(\Delta_4) \\ t & t & t & \rho_3(\Delta_4) & \rho_2(\Delta_4) & \rho_1(\Delta_4) \end{pmatrix}. \tag{29}$$

Here, the matrix elements are defined as

$$\rho_1(\Delta) = \tfrac{1}{3}(\Delta + \Delta^*), \tag{30a}$$

$$\rho_2(\Delta) = \tfrac{1}{3}\left(e^{i\frac{2\pi}{3}}\Delta + e^{-i\frac{2\pi}{3}}\Delta^*\right), \tag{30b}$$

$$\rho_3(\Delta) = \tfrac{1}{3}\left(e^{-i\frac{2\pi}{3}}\Delta + e^{i\frac{2\pi}{3}}\Delta^*\right) \tag{30c}$$

for $\Delta = \Delta_3$ or Δ_4. This perturbed Hamiltonian shows that nonzero on-site energies are introduced to the system, while the sum of all on-site energies is zero because $\rho_1(\Delta) + \rho_2(\Delta) + \rho_3(\Delta) = 0$ for any Δ. In addition, while the nearest-neighbor interaction is not changed, nonzero next-nearest-neighbor interactions are introduced within each sublattice with an assumed 120° rotational symmetry around each perturbed site. These hopping matrix elements are visualized in Fig. 4(a). Extending this Hamiltonian at Γ to a k point in the BZ gives

$$H_{sc}(\vec{k}) = \begin{pmatrix} \rho_2(\Delta_3) & \frac{\rho_3(\Delta_3)f(-\vec{k})}{3} & \frac{\rho_1(\Delta_3)f(\vec{k})}{3} & te^{i\vec{k}\cdot\vec{d}_1} & te^{i\vec{k}\cdot\vec{d}_2} & te^{i\vec{k}\cdot\vec{d}_3} \\ \frac{\rho_3(\Delta_3)f(\vec{k})}{3} & \rho_1(\Delta_3) & \frac{\rho_2(\Delta_3)f(-\vec{k})}{3} & te^{i\vec{k}\cdot\vec{d}_2} & te^{i\vec{k}\cdot\vec{d}_3} & te^{i\vec{k}\cdot\vec{d}_1} \\ \frac{\rho_1(\Delta_3)f(-\vec{k})}{3} & \frac{\rho_2(\Delta_3)f(\vec{k})}{3} & \rho_3(\Delta_3) & te^{i\vec{k}\cdot\vec{d}_3} & te^{i\vec{k}\cdot\vec{d}_1} & te^{i\vec{k}\cdot\vec{d}_2} \\ te^{-i\vec{k}\cdot\vec{d}_1} & te^{-i\vec{k}\cdot\vec{d}_2} & te^{-i\vec{k}\cdot\vec{d}_3} & \rho_2(\Delta_4) & \frac{\rho_1(\Delta_4)f(\vec{k})}{3} & \frac{\rho_3(\Delta_4)f(-\vec{k})}{3} \\ te^{-i\vec{k}\cdot\vec{d}_2} & te^{-i\vec{k}\cdot\vec{d}_3} & te^{-i\vec{k}\cdot\vec{d}_1} & \frac{\rho_1(\Delta_4)f(-\vec{k})}{3} & \rho_3(\Delta_4) & \frac{\rho_2(\Delta_4)f(\vec{k})}{3} \\ te^{-i\vec{k}\cdot\vec{d}_3} & te^{-i\vec{k}\cdot\vec{d}_1} & te^{-i\vec{k}\cdot\vec{d}_2} & \frac{\rho_3(\Delta_4)f(\vec{k})}{3} & \frac{\rho_2(\Delta_4)f(-\vec{k})}{3} & \rho_1(\Delta_4) \end{pmatrix}. \tag{31}$$

The band structure obtained from the Hamiltonian (31) with $\Delta_3 = e^{-i\frac{2\pi}{3}}\Delta_4$ and $\Delta_4 = 1$ eV shows that the Dirac cones are simply shifted from their original positions in the BZ toward K_S and K'_S points, maintaining the shapes of the cones without opening an energy gap at the Dirac point, as shown in Figs. 4(b) and 4(c).

D. Coexistence of the sublattice mixing without intervalley scattering and the intervalley scattering within each sublattice

In this section, we consider a perturbation which produces sublattice mixing without intervalley scattering and intervalley scattering within each sublattice simultaneously. The ξ-basis Hamiltonian with the perturbation is

$$\mathcal{H}_{sc}^{(\xi)} = \begin{pmatrix} 0 & \Delta_3 & \Delta_1 & 0 & 0 & 0 \\ \Delta_3^* & 0 & 0 & \Delta_2 & 0 & 0 \\ \Delta_1^* & 0 & 0 & \Delta_4 & 0 & 0 \\ 0 & \Delta_2^* & \Delta_4^* & 0 & 0 & 0 \\ 0 & 0 & 0 & 0 & 0 & 3t \\ 0 & 0 & 0 & 0 & 3t & 0 \end{pmatrix}. \tag{32}$$

Using the unitary transformation from the ξ to the $\tilde{\varphi}$ basis, that is, $[H_{sc}(\vec{k}=0)]_{ij} = \sum_{m,n} U_{im}(\mathcal{H}_{sc}^{(\xi)})_{mn}U_{jn}^*$, we have

$$H_{sc}(\vec{k}=0) = \begin{pmatrix} \rho_2(\Delta_3) & \rho_3(\Delta_3) & \rho_1(\Delta_3) & \lambda_1+t & \lambda_2+t & \lambda_3+t \\ \rho_3(\Delta_3) & \rho_1(\Delta_3) & \rho_2(\Delta_3) & \lambda_2+t & \lambda_3+t & \lambda_1+t \\ \rho_1(\Delta_3) & \rho_2(\Delta_3) & \rho_3(\Delta_3) & \lambda_3+t & \lambda_1+t & \lambda_2+t \\ \lambda_1^*+t & \lambda_2^*+t & \lambda_3^*+t & \rho_2(\Delta_4) & \rho_1(\Delta_4) & \rho_3(\Delta_4) \\ \lambda_2^*+t & \lambda_3^*+t & \lambda_1^*+t & \rho_1(\Delta_4) & \rho_3(\Delta_4) & \rho_2(\Delta_4) \\ \lambda_3^*+t & \lambda_1^*+t & \lambda_2^*+t & \rho_3(\Delta_4) & \rho_2(\Delta_4) & \rho_1(\Delta_4) \end{pmatrix}, \tag{33}$$

where $\lambda_{i=1,2,3}$ are functions of Δ_1 and Δ_2 as defined by Eq. (26) and $\rho_{i=1,2,3}(\Delta)$ are the same as defined by Eq. (30). Extending this Hamiltonian at Γ to a k point in the BZ gives

$$H_{sc}(\vec{k}) = \begin{pmatrix} \rho_2(\Delta_3) & \frac{\rho_3(\Delta_3)f(-\vec{k})}{3} & \frac{\rho_1(\Delta_3)f(\vec{k})}{3} & (\lambda_1+t)e^{i\vec{k}\cdot\vec{d}_1} & (\lambda_2+t)e^{i\vec{k}\cdot\vec{d}_2} & (\lambda_3+t)e^{i\vec{k}\cdot\vec{d}_3} \\ \frac{\rho_3(\Delta_3)f(\vec{k})}{3} & \rho_1(\Delta_3) & \frac{\rho_2(\Delta_3)f(-\vec{k})}{3} & (\lambda_2+t)e^{i\vec{k}\cdot\vec{d}_2} & (\lambda_3+t)e^{i\vec{k}\cdot\vec{d}_3} & (\lambda_1+t)e^{i\vec{k}\cdot\vec{d}_1} \\ \frac{\rho_1(\Delta_3)f(-\vec{k})}{3} & \frac{\rho_2(\Delta_3)f(\vec{k})}{3} & \rho_3(\Delta_3) & (\lambda_3+t)e^{i\vec{k}\cdot\vec{d}_3} & (\lambda_1+t)e^{i\vec{k}\cdot\vec{d}_1} & (\lambda_2+t)e^{i\vec{k}\cdot\vec{d}_2} \\ (\lambda_1^*+t)e^{-i\vec{k}\cdot\vec{d}_1} & (\lambda_2^*+t)e^{-i\vec{k}\cdot\vec{d}_2} & (\lambda_3^*+t)e^{-i\vec{k}\cdot\vec{d}_3} & \rho_2(\Delta_4) & \frac{\rho_1(\Delta_4)f(\vec{k})}{3} & \frac{\rho_3(\Delta_4)f(-\vec{k})}{3} \\ (\lambda_2^*+t)e^{-i\vec{k}\cdot\vec{d}_2} & (\lambda_3^*+t)e^{-i\vec{k}\cdot\vec{d}_3} & (\lambda_1^*+t)e^{-i\vec{k}\cdot\vec{d}_1} & \frac{\rho_1(\Delta_4)f(-\vec{k})}{3} & \rho_3(\Delta_4) & \frac{\rho_2(\Delta_4)f(\vec{k})}{3} \\ (\lambda_3^*+t)e^{-i\vec{k}\cdot\vec{d}_3} & (\lambda_1^*+t)e^{-i\vec{k}\cdot\vec{d}_1} & (\lambda_2^*+t)e^{-i\vec{k}\cdot\vec{d}_2} & \frac{\rho_3(\Delta_4)f(\vec{k})}{3} & \frac{\rho_2(\Delta_4)f(-\vec{k})}{3} & \rho_1(\Delta_4) \end{pmatrix}. \tag{34}$$

Figures 5(a)–5(c) show calculational results using this Hamiltonian with $\Delta_2 = \Delta_4 = 1$ eV and $\Delta_1 = \Delta_3 = e^{-i\frac{2\pi}{3}}\Delta_2$. With the perturbation, two bands with quadratic dispersion touch at the Fermi energy without a gap opening, as shown in Fig. 5(c). With $\Delta_2 = \Delta_4 = \Delta$ and $\Delta_1 = \Delta_3 = e^{-i\frac{2\pi}{3}}\Delta$, the effective mass of the upper quadratic band is obtained and plotted as a function of the perturbation strength Δ in Fig. 5(d).

E. Intersublattice intervalley scattering

We further consider a perturbation which produces intersublattice intervalley scattering. The ξ-basis perturbed Hamiltonian is

$$\mathcal{H}_{sc}^{(\xi)} = \begin{pmatrix} 0 & 0 & 0 & \Delta_1 & 0 & 0 \\ 0 & 0 & \Delta_2 & 0 & 0 & 0 \\ 0 & \Delta_2^* & 0 & 0 & 0 & 0 \\ \Delta_1^* & 0 & 0 & 0 & 0 & 0 \\ 0 & 0 & 0 & 0 & 0 & 3t \\ 0 & 0 & 0 & 0 & 3t & 0 \end{pmatrix}. \tag{35}$$

Here, the four states $\xi_{A,K}$, $\xi_{A,K'}$, $\xi_{B,K}$, and $\xi_{B,K'}$ are mixed between different K points and different sublattices simultaneously. By the unitary transformation $[H_{sc}(\vec{k}=0)]_{ij} = \sum_{m,n} U_{im}(\mathcal{H}_{sc}^{(\xi)})_{mn}U_{jn}^*$, we express the Hamiltonian using the $\tilde{\varphi}$ basis as

$$H_{sc}(\vec{k}=0) = \begin{pmatrix} 0 & 0 & 0 & \lambda_2+t & \lambda_1+t & \lambda_3+t \\ 0 & 0 & 0 & \lambda_3+t & \lambda_2+t & \lambda_1+t \\ 0 & 0 & 0 & \lambda_1+t & \lambda_3+t & \lambda_2+t \\ \lambda_2^*+t & \lambda_3^*+t & \lambda_1^*+t & 0 & 0 & 0 \\ \lambda_1^*+t & \lambda_2^*+t & \lambda_3^*+t & 0 & 0 & 0 \\ \lambda_3^*+t & \lambda_1^*+t & \lambda_2^*+t & 0 & 0 & 0 \end{pmatrix}, \tag{36}$$

where $\lambda_{i=1,2,3}$ are functions of Δ_1 and Δ_2 as defined by Eq. (26) in Sec. III B. We note that λ_i are positioned differently in matrix (36) compared with matrices (25), (27), (33), and (34). The parameters Δ_1 and Δ_2 are complex numbers in general, but they should satisfy the constraint that all λ_i are real. Extending the Hamiltonian (36) at the Γ point to a k point in the BZ gives

$$H_{sc}(\vec{k}) = \begin{pmatrix} 0 & 0 & 0 & (\lambda_2+t)e^{i\vec{k}\cdot\vec{d}_1} & (\lambda_1+t)e^{i\vec{k}\cdot\vec{d}_2} & (\lambda_3+t)e^{i\vec{k}\cdot\vec{d}_3} \\ 0 & 0 & 0 & (\lambda_3+t)e^{i\vec{k}\cdot\vec{d}_2} & (\lambda_2+t)e^{i\vec{k}\cdot\vec{d}_3} & (\lambda_1+t)e^{i\vec{k}\cdot\vec{d}_1} \\ 0 & 0 & 0 & (\lambda_1+t)e^{i\vec{k}\cdot\vec{d}_3} & (\lambda_3+t)e^{i\vec{k}\cdot\vec{d}_1} & (\lambda_2+t)e^{i\vec{k}\cdot\vec{d}_2} \\ (\lambda_2^*+t)e^{-i\vec{k}\cdot\vec{d}_1} & (\lambda_3^*+t)e^{-i\vec{k}\cdot\vec{d}_2} & (\lambda_1^*+t)e^{-i\vec{k}\cdot\vec{d}_3} & 0 & 0 & 0 \\ (\lambda_1^*+t)e^{-i\vec{k}\cdot\vec{d}_2} & (\lambda_2^*+t)e^{-i\vec{k}\cdot\vec{d}_3} & (\lambda_3^*+t)e^{-i\vec{k}\cdot\vec{d}_1} & 0 & 0 & 0 \\ (\lambda_3^*+t)e^{-i\vec{k}\cdot\vec{d}_3} & (\lambda_1^*+t)e^{-i\vec{k}\cdot\vec{d}_1} & (\lambda_2^*+t)e^{-i\vec{k}\cdot\vec{d}_2} & 0 & 0 & 0 \end{pmatrix}. \quad (37)$$

Thus the perturbed graphene has variation in the nearest-neighbor hopping energies, as shown in Fig. 6(a).

Figures 6(b) and 6(c) show the electronic band structure obtained from this perturbed Hamiltonian with $\Delta_1 = e^{-i\frac{2\pi}{3}}\Delta_2$ and $\Delta_2 = 1$ eV. With the perturbation strength Δ such that $\Delta_1 = e^{-i\frac{2\pi}{3}}\Delta$ and $\Delta_2 = \Delta$, the energy gap E_g is 2Δ, and the effective mass of the lowest conduction band at Γ, defined as Eq. (22), increases as the band gap increases, as shown in Fig. 6(e). By analytic calculation, we can derive

$$m^* = \frac{12\hbar^2 E_g}{|\vec{a}_1|^2(6t - E_g)(3t + E_g)}, \quad (38)$$

which is in good agreement with the numerical results shown in Fig. 6(e).

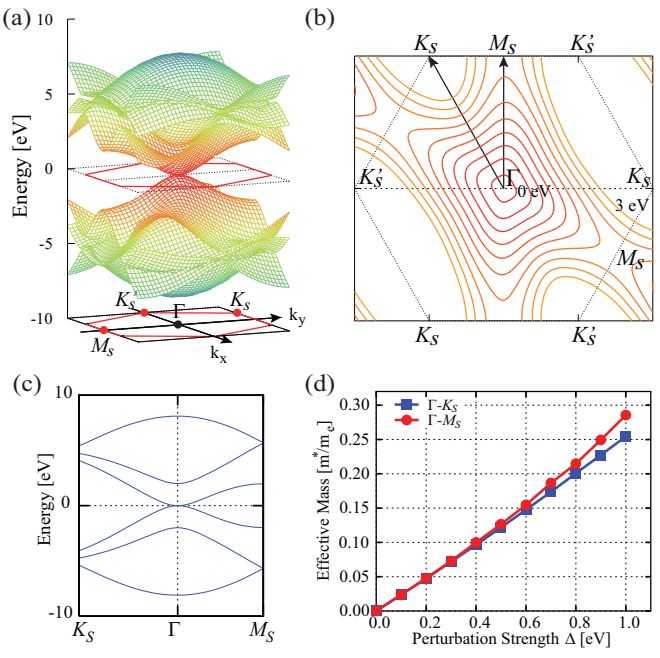

FIG. 5. (Color online) Graphene with both the sublattice mixing without intervalley scattering and the intervalley scattering within each sublattice. (a) Tight-binding band structure of perturbed graphene in the full BZ of the supercell when $\Delta_1 = \Delta_3 = e^{-i\frac{2\pi}{3}}\Delta_2$ and $\Delta_2 = \Delta_4 = 1$ eV in the Hamiltonian (34). (Δ_1 and Δ_3 are complex and Δ_2 and Δ_4 are real.) (b) Contour plot of the lowest conduction band from 0 to 3 eV with a contour interval of 0.3 eV. Arrows indicate high-symmetry lines for (c) and (d). (c) Tight-binding band structure of perturbed graphene along high-symmetry lines. (d) The effective mass of the lowest conduction band at Γ as a function of the perturbation strength Δ when $\Delta_1 = \Delta_3 = e^{-i\frac{2\pi}{3}}\Delta$ and $\Delta_2 = \Delta_4 = \Delta$. The effective mass is slightly different in the Γ-K_S and Γ-M_S directions.

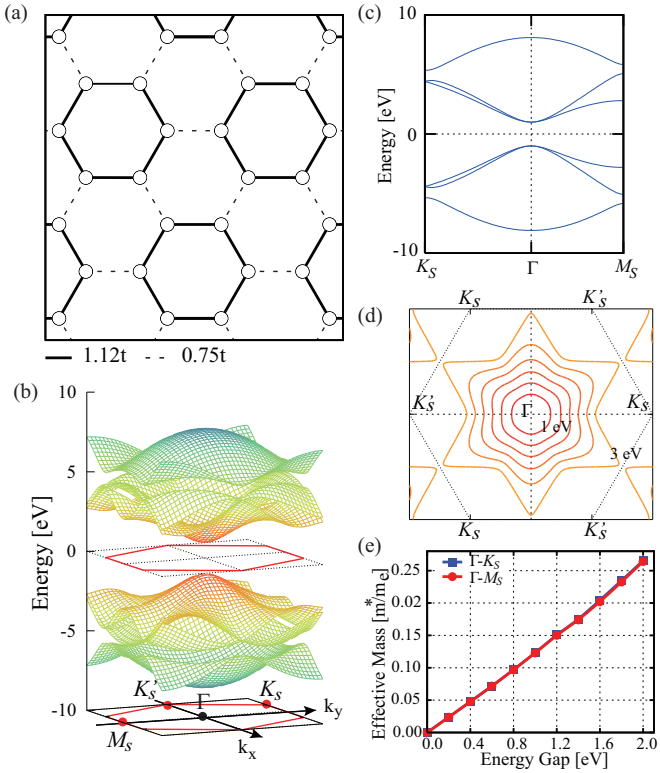

FIG. 6. (Color online) Graphene with the intersublattice intervalley scattering. (a) Schematic representation of the perturbed Hamiltonian (37) with $\Delta_1 = e^{-i\frac{2\pi}{3}}\Delta_2$ and $\Delta_2 = 1$ eV. (Δ_1 is complex and Δ_2 is real.) The solid and dashed lines show variation of the nearest-neighbor hopping matrix elements, which are $1.12t$ and $0.75t$, respectively. (b) Tight-binding band structure of perturbed graphene in the full BZ of the supercell. (c) Tight-binding band structure of perturbed graphene along high-symmetry lines. (d) Contour plot of the lowest conduction band from 1 to 3 eV with a contour interval of 0.3 eV. (e) The effective mass of the lowest conduction band at Γ as a function of the energy gap (=2Δ). The effective mass in the Γ-K_S direction is the same as that in the Γ-M_S direction.

If we apply strain with 120° rotational symmetry [46], we may introduce the variation in hopping matrix elements with the symmetry shown in Fig. 6(a). This type of perturbation is often called as Kekulé distortion [31,33,47]. As can be seen from the calculated band structure, such a distortion results in a band-gap opening in the graphene system. A similar band-gap opening also occurs in nitrogenated holey two-dimensional carbon structures [48] and in graphyne [49].

IV. SUMMARY

In our present work, we classified perturbations to graphene and investigated their effects on the electronic structures using a simple tight-binding method. We distinguished different types of perturbations: (a) the sublattice symmetry breaking without intervalley scattering, (b) the sublattice mixing without intervalley scattering, (c) the intervalley scattering within each sublattice, (d) the coexistence of the sublattice mixing without intervalley scattering and the intervalley scattering within each sublattice, and (e) the intersublattice intervalley scattering. Our approach shows that the energy gap is opened by the sublattice symmetry breaking without intervalley scattering and by the the intersublattice intervalley scattering. When such perturbations open an energy gap, the charge carriers have nonzero effective mass which increases as the energy gap increases. This suggests that when a band gap opens in graphene, the mobility of the charge carriers may inevitably decrease because of the increase of the effective mass.

Our results also show that when the sublattice mixing occurs without intervalley scattering, graphene is still metallic, although the Dirac cones are shifted in k space and the shapes of the cones are deformed. In addition, when the intervalley scattering occurs without sublattice mixing, graphene is metallic, although the Dirac cones are shifted in k space, maintaining the isotropy of the cones. Even when the sublattice mixing without intervalley scattering and the intervalley scattering within each sublattice occur simultaneously, graphene is metallic, although the band dispersion at the Dirac point changes from the linear one to the quadratic.

Our present work is to introduce perturbations directly in the small Hilbert space at the Dirac point of graphene and to obtain the band structure throughout the BZ. This approach provides a very straightforward theoretical framework for classification and analysis of perturbations to graphene, and it is applicable to band-gap engineering of graphene-like hexagonal layered materials in general.

ACKNOWLEDGMENT

This work was supported by the National Research Foundation of Korea (Grant No. 2011-0018306).

[1] A. K. Geim and K. S. Novoselov, Nat. Mater. **6**, 183 (2007).
[2] K. S. Novoselov, A. K. Geim, S. V. Morozov, D. Jiang, Y. Zhang, S. V. Dubonos, I. V. Grigorieva, and A. A. Firsov, Science **306**, 666 (2004).
[3] Y. Zhang, Y. W. Tan, H. L. Stormer, and P. Kim, Nature (London) **438**, 201 (2005).
[4] K. S. Novoselov, A. K. Geim, S. V. Morozov, D. Jiang, M. I. Katsnelson, I. V. Grigorieva, S. V. Dubonos, and A. A. Firsov, Nature (London) **438**, 197 (2005).
[5] F. D. M. Haldane, Phys. Rev. Lett. **61**, 2015 (1988).
[6] G. W. Semenoff, Phys. Rev. Lett. **53**, 2449 (1984).
[7] C. L. Kane and E. J. Mele, Phys. Rev. Lett. **95**, 146802 (2005).
[8] Y. Zheng and T. Ando, Phys. Rev. B **65**, 245420 (2002).
[9] D. P. DiVincenzo and E. J. Mele, Phys. Rev. B **29**, 1685 (1984).
[10] P. R. Wallace, Phys. Rev. **71**, 622 (1947).
[11] A. H. Castro Neto, F. Guinea, N. M. R. Peres, K. S. Novoselov, and A. K. Geim, Rev. Mod. Phys. **81**, 109 (2009).
[12] C. Priester, G. Allan, and J. Conard, Phys. Rev. B **26**, 4680 (1982).
[13] J. L. McChesney, A. Bostwick, T. Ohta, T. Seyller, K. Horn, J. González, and E. Rotenberg, Phys. Rev. Lett. **104**, 136803 (2010).
[14] S. Kim, J. Ihm, H. J. Choi, and Y.-W. Son, Phys. Rev. Lett. **100**, 176802 (2008).
[15] P. Shemella and S. K. Nayak, Appl. Phys. Lett. **94**, 032101 (2009).
[16] Y. Guo, W. Guo, and C. Chen, Phys. Rev. B **80**, 085424 (2009).
[17] H. Lee, S. Kim, J. Ihm, Y.-W. Son, and H. J. Choi, Carbon **49**, 2300 (2011).
[18] S. Kim, J. Ihm, H. J. Choi, and Y.-W. Son, Solid State Commun. **175-176**, 83 (2013).
[19] T. G. Pedersen, C. Flindt, J. Pedersen, N. A. Mortensen, A.-P. Jauho, and K. Pedersen, Phys. Rev. Lett. **100**, 136804 (2008).
[20] C.-H. Park, L. Yang, Y.-W. Son, M. L. Cohen, and S. G. Louie, Nat. Phys. **4**, 213 (2008).
[21] B. Gharekhanlou, M. Alavi, and S. Khorasani, Semicond. Sci. Technol. **23**, 075026 (2008).
[22] A. Sinitskii and J. M. Tour, J. Am. Chem. Soc. **132**, 14730 (2010).
[23] R. Balog, B. Jørgensen, L. Nilsson, M. Andersen, E. Rienks, M. Bianchi, M. Fanetti, E. Lægsgaard, A. Baraldi, S. Lizzit, Z. Sljivancanin, F. Besenbacher, B. Hammer, T. G. Pedersen, P. Hofmann, and L. Honekær, Nat. Mater. **9**, 315 (2010).
[24] J. Schelter, P. M. Ostrovsky, I. V. Gornyi, B. Trauzettel, and M. Titov, Phys. Rev. Lett. **106**, 166806 (2011).
[25] K. Novoselov, Nat. Mater. **6**, 720 (2007).
[26] S. Y. Zhou, G.-H. Gweon, A. V. Fedorov, P. N. First, W. A. De Heer, D.-H. Lee, F. Guinea, A. H. Castro Neto, and L. Lanzara, Nat. Mater. **6**, 770 (2007).
[27] G. M. Rutter, J. N. Crain, N. P. Guisinger, T. Li, P. N. First, and J. A. Stroscio, Science **317**, 219 (2007).
[28] I. Brihuega, P. Mallet, C. Bena, S. Bose, C. Michaelis, L. Vitali, F. Varchon, L. Magaud, K. Kern, and J. Y. Veuillen, Phys. Rev. Lett. **101**, 206802 (2008).
[29] G. Giovannetti, P. A. Khomyakov, G. Brocks, P. J. Kelly, and J. van den Brink, Phys. Rev. B **76**, 073103 (2007).
[30] B. Sachs, T. O. Wehling, M. I. Katsnelson, and A. I. Lichtenstein, Phys. Rev. B **84**, 195414 (2011).
[31] C. Chamon, Phys. Rev. B **62**, 2806 (2000).

[32] C.-Y. Hou, C. Chamon, and C. Mudry, Phys. Rev. Lett. **98**, 186809 (2007).
[33] S.-H. Lee, H.-J. Chung, J. Heo, H. Yang, J. Shin, U-In Chung, and S. Seo, ACS Nano **5**, 2964 (2011).
[34] J. L. Mañes, F. Guinea, and M. A. H. Vozmediano, Phys. Rev. B **75**, 155424 (2007).
[35] J. L. Mañes, Phys. Rev. B **76**, 045430 (2007).
[36] N. W. Ashcroft and N. D. Mermin, *Solid State Physics* (Brooks/Cole Cengage Learning, Belmont, CA, 1976).
[37] S. Casolo, R. Martinazzo, and G. F. Tantardini, J. Phys. Chem. C **115**, 3250 (2011).
[38] T. Ando, Y. Zheng, and H. Suzuura, J. Phys. Soc. Jpn. **71**, 1318 (2002).
[39] S. Reich, J. Maultzsch, C. Thomsen, and P. Ordejón, Phys. Rev. B **66**, 035412 (2002).
[40] R. Saito, G. Dresselhaus, and M. S. Dresselhaus, *Physical Properties of Carbon Nanotubes* (Imperial College Press, London, 1998).
[41] L. S. Braginsky and M. V. Entin, JETP Lett. **101**, 325 (2015).
[42] M. M. Fogler, F. Guinea, and M. I. Katsnelson, Phys. Rev. Lett. **101**, 226804 (2008).
[43] W. Bao, F. Miao, Z. Chen, H. Zhang, W. Jang, C. Dames, and C. N. Lau, Nat. Nanotechnol. **4**, 562 (2009).
[44] T. M. G. Mohiuddin, A. Lombardo, R. R. Nair, A. Bonetti, G. Savini, R. Jalil, N. Bonini, D. M. Basko, C. Galiotis, N. Marzari, K. S. Novoselov, A. K. Geim, and A. C. Ferrari, Phys. Rev. B **79**, 205433 (2009).
[45] V. M. Pereira, A. H. Castro Neto, and N. M. R. Peres, Phys. Rev. B **80**, 045401 (2009).
[46] F. Guinea, M. I. Katsnelson, and A. K. Geim, Nat. Phys. **6**, 30 (2010).
[47] Ge. G. Samsonidze, E. B. Barros, R. Saito, J. Jiang, G. Dresselhaus, and M. S. Dresselhaus, Phys. Rev. B **75**, 155420 (2007).
[48] J. Mahmood, E. K. Lee, M. Jung, D. Shin, I.-Y. Jeon, S.-M. Jung, H.-J. Choi, J.-M. Seo, S.-Y. Bae, S.-D. Sohn, N. Park, J. H. Oh, H.-J. Shin, and J.-B. Baek, Nat. Commun. **6**, 6486 (2015).
[49] B. G. Kim and H. J. Choi, Phys. Rev. B **86**, 115435 (2012).